

Observation of a gel of quantum vortices in a superconductor at very low magnetic fields

José Benito Llorens,¹ Lior Embon,² Alexandre Correa,³ Jesús David González,^{4,5} Edwin Herrera,^{1,6} Isabel Guillamón,^{1,7} Roberto F. Luccas,^{3,8} Jon Azpeitia,³ Federico J. Mompeán,^{3,7} Mar García-Hernández,^{3,7} Carmen Munuera,^{3,7} Jazmín Aragón Sánchez,⁹ Yanina Fasano,⁹ Milorad V. Milošević,⁵ Hermann Suderow,^{1,7} and Yonathan Anahory^{10,2}

¹*Laboratorio de Bajas Temperaturas, Departamento de Física de la Materia Condensada, Instituto Nicolás Cabrera and Condensed Matter Physics Center (IFIMAC), Universidad Autónoma de Madrid, E-28049 Madrid, Spain*

²*Department of Condensed Matter Physics, Weizmann Institute of Science, Rehovot 76100, Israel*

³*Instituto de Ciencia de Materiales de Madrid, Consejo Superior de Investigaciones Científicas (ICMM-CSIC), Sor Juana Inés de la Cruz 3, 28049 Madrid, Spain*

⁴*Facultad de ingeniería, Universidad del Magdalena, Santa Marta, Colombia*

⁵*Theory of Functional Materials, Department of Physics,*

University of Antwerp, Groenenborgerlaan 171, B-2020 Antwerpen, Belgium

⁶*Facultad de Ingeniería y Ciencias Básicas, Universidad Central, Bogotá 110311, Colombia.*

⁷*Unidad Asociada de Bajas Temperaturas y Altos Campos Magnéticos, UAM, CSIC, Cantoblanco, E-28049 Madrid, Spain*

⁸*Instituto de Física Rosario, CONICET-UNR, Bv. 27 de Febrero 210bis, S2000EZF Rosario, Santa Fé, Argentina.*

⁹*Centro Atómico Bariloche and Instituto Balseiro, CNEA and Universidad de Cuyo, Av. E. Bustillo 9500, R8402AGP, S. C. Bariloche, RN, Argentina*

¹⁰*Racah Institute of Physics, The Hebrew University, Jerusalem 91904, Israel*

(Dated: June 23, 2022)

A gel consists of a network of particles or molecules formed for example by the sol-gel process, by which a solution transforms into a porous solid. Particles or molecules in a gel are mainly organized on a scaffold that makes up a porous system. Quantized vortices in type II superconductors can freeze into an amorphous solid, particularly at low magnetic fields where vortices are nearly noninteracting. Here we present high-resolution imaging of the vortex lattice displaying dense vortex clusters separated by sparse or entirely vortex-free regions in β -Bi₂Pd superconductor containing one-dimensional structural defects. In contrast to the amorphous state, we find that the vortex distribution follows a multifractal behavior and the variance of intervortex distances diverges upon decreasing the magnetic field. These properties, characteristic of gels, establish the presence of a novel vortex matter phase, distinctly different from the well-studied disordered and glassy phases observed in high-temperature and conventional superconductors. The vortex gel is expected to be generic to type-II superconductors at low magnetic fields containing strained extended defects, which could be engineered for isolating and manipulating clusters of quantum vortex states.

INTRODUCTION

Quantized vortices in superconductors arrange themselves spatially in structures that bear some similarities with atomic or molecular arrangements. The main difference is that vortices are simple structures, mostly consisting of single quantized fluxes, whereas atoms and molecules have numerous degrees of freedom for bonding. Nevertheless, interactions among vortices can also be varied because these are related to the properties of the superconducting material hosting them^{1,2}. Thus, solid, liquid or disordered glass phases, have been observed in vortex matter³⁻⁵. However, a gel with inhomogeneous density distribution caused by a network has not yet been reported in vortex matter. Such a phase might eventually exist at very low magnetic fields, where vortices are nearly independent from each other. Experiments made in superconductors at low magnetic fields have until now unveiled different phenomena, such as hexagonal polycrystalline vortex arrangements, vortex clustering due

to attractive interactions or glassy phases⁵⁻¹⁶. But the vortex density mostly remained spatially homogeneous. Here we image the vortex configurations at very low magnetic fields in the single-gap isotropic s-wave superconductor β -Bi₂Pd. We find vortex clusters whose distribution has characteristics specific to gels, such as large separation between clusters and multifractal distributions. High-resolution magnetic imaging allows us to attribute this new kind of vortex distribution to pinning. β -Bi₂Pd crystallizes in a tetragonal structure and becomes superconducting below $T_c \approx 5$ K^{17,18}. Zero-temperature critical magnetic fields are $H_{c1} = 225$ Oe and $H_{c2} = 6000$ Oe (yielding coherence length $\xi(0) \approx 23.5$ nm and penetration depth $\lambda(0) \approx 132$ nm). The upper critical field anisotropy is small, of order of 10%^{18,19}. Single crystals of this material can be easily cleaved, leaving large stable and atomically flat terraces, where a fully formed s-wave superconducting gap is observed over the entire surface¹⁸. We have carefully analyzed the fracture produced when cleaving the sample and observed a network of defects that organizes in linear features (see Supple-

mentary Note 1). More details about the materials are provided in Supplementary Note 2. Here we undertook a thorough examination of vortex states using squid-on-tip (SOT) microscopy^{20,21} and magnetic force microscopy (MFM)²² in a large range of magnetic fields, from 1 to 600 Oe.

RESULTS

In Fig. 1a we show a $7 \times 7 \mu\text{m}^2$ AFM image taken at 2 K. We observe flat surfaces interspersed with steps of 10 nm height or larger. The vortex lattice shown in Fig. 1b is measured simultaneously with MFM at 300 Oe. In Fig. 1c shows a image of the local magnetic field $B(x, y)$ acquired using the SOT. Further details on the MFM and SOT experimental set-ups are provided in the Methods. In Fig. 1d-i we show SOT images between 2 and 50 Oe taken in field-cooled conditions at 4.2 K. At low magnetic fields, Fig. 1d,e, many vortices are located along one dominant line, while, in the rest of the frame, we observe large vortex-free regions. When increasing the magnetic field, vortices cluster along lines and the vortex lattice is formed in between (Fig. 1f-i).

Note that for vortices located along lines, the value of the magnetic field at the vortex center is smaller than the value we find for vortices located far from lines. This is nicely visible at low fields when vortices are well separated and do not overlap. For example, in Fig. 1d we see that vortices located along the main linear defect visible in the image (from upper left to middle right) are not as bright as those located elsewhere in the image. This remains in the whole range of magnetic fields (in Fig. 1f-i there is strong vortex overlap, which produces linear vortex clusters that appear very bright). When we fit the spatial profile of vortices along lines in the images at low fields we find values for λ close to 340 ± 40 nm, which is about twice the penetration depth found in experiments measuring bulk field penetration with Hall probes¹⁹. More details on the fitting procedure are given in Supplementary Note 3.

We have made numerical simulations of vortex behavior close to linear defects using Ginzburg-Landau theory. We parametrize the simulations according to the values of λ measured, that are translated into small changes of T_c close to the defects and weak disorder (i.e. a randomized value of T_c). The behavior close to the linear defect is modeled through a parabolic recovery of T_c at a distance of $2 \mu\text{m}$ away from the step. This simulates the pinning potential of the linear defect. The obtained vortex configurations over a $10 \times 20 \mu\text{m}^2$ area are shown in Fig. 2, for three values of applied magnetic field. This indeed captures the evolution seen in the images. Namely, vortices first occupy locations along the defect, where superconductivity is suppressed, and their magnetic field is weaker than that of vortices found away from the defect. The accumulation of vortices at the defect strengthens repulsion of other vortices in the sample, so that a no-

ticeable vortex-free band is formed between vortices of different brightness in the images. The vortex free band diminishes with increasing magnetic field.

The more striking result appears at the smallest magnetic fields. There, vortices are located along lines separated by large vortex free areas (Fig. 1d). We have Delaunay triangulated images and calculated intervortex distances. In Fig. 3a we show intervortex distance histograms and in Fig. 3b the standard deviation of intervortex distances. First of all, let us remark that all distance histograms (Fig. 3a) show just a single peak located at $a_0 = (\frac{4}{3})^{1/4} (\frac{\Phi_0}{B})^{1/2}$ for all magnetic fields. This means that the average intervortex distance follows the Abrikosov rule for a triangular lattice. The magnetic field behavior of the position of this peak is shown in the inset of Fig. 3b and we can see that its value coincides with a_0 also at the weakest magnetic fields. This includes situations where vortices are strongly clustered with large voids in between clusters. At the weakest magnetic fields, the histograms of Fig. 3a are extremely broad and the distances between vortices become wide-spread. We observe intervortex distances d up to twice a_0 and many vortices located much closer to each other than a_0 . The standard deviation of the histograms as a function of the magnetic field (Fig. 3b) diverges as $1/\sqrt{\mu_0 H}$ below about 80 Oe.

We compare our results with distance histograms obtained in the same range of magnetic fields in a cuprate superconductor, $\text{Bi}_2\text{Sr}_2\text{CaCu}_2\text{O}_8$ in the cases of pristine samples and crystals with a strong and dense distribution of pinning centers (columnar defects)²³. In both cases the vortex density is much more homogeneous than in β - Bi_2Pd and the standard deviation remains constant when decreasing the magnetic field (black and violet points in Fig. 3b).

DISCUSSION

All our experiments are in field-cooled conditions, so during cooling, vortices are nucleated inside the sample. Clearly, our data shows that there are locations with vortex pinning determined by linear defects, which provide a scaffold to pin vortices at low magnetic fields and areas in between that remain vortex free.

Vortices located on the scaffold have a different λ . We consider stress as a possible mechanism to explain the spatial variation of λ . Stress builds up close to defects and modifies the superconducting length scales (and the Ginzburg-Landau parameter), producing an effective interaction between the crystal lattice and the vortex lattice^{24,25}. Recently, it has been shown that stress induced intervortex interaction can lead to square vortex lattice in tetragonal superconductors²⁶. Such a coupling between crystalline elasticity and superconductivity can be treated using the dependence of T_c with pressure, dT_c/dP ^{24,27-29}. Generally, with $dT_c/dP > 0$, vortices are repelled from places with internal stress and the op-

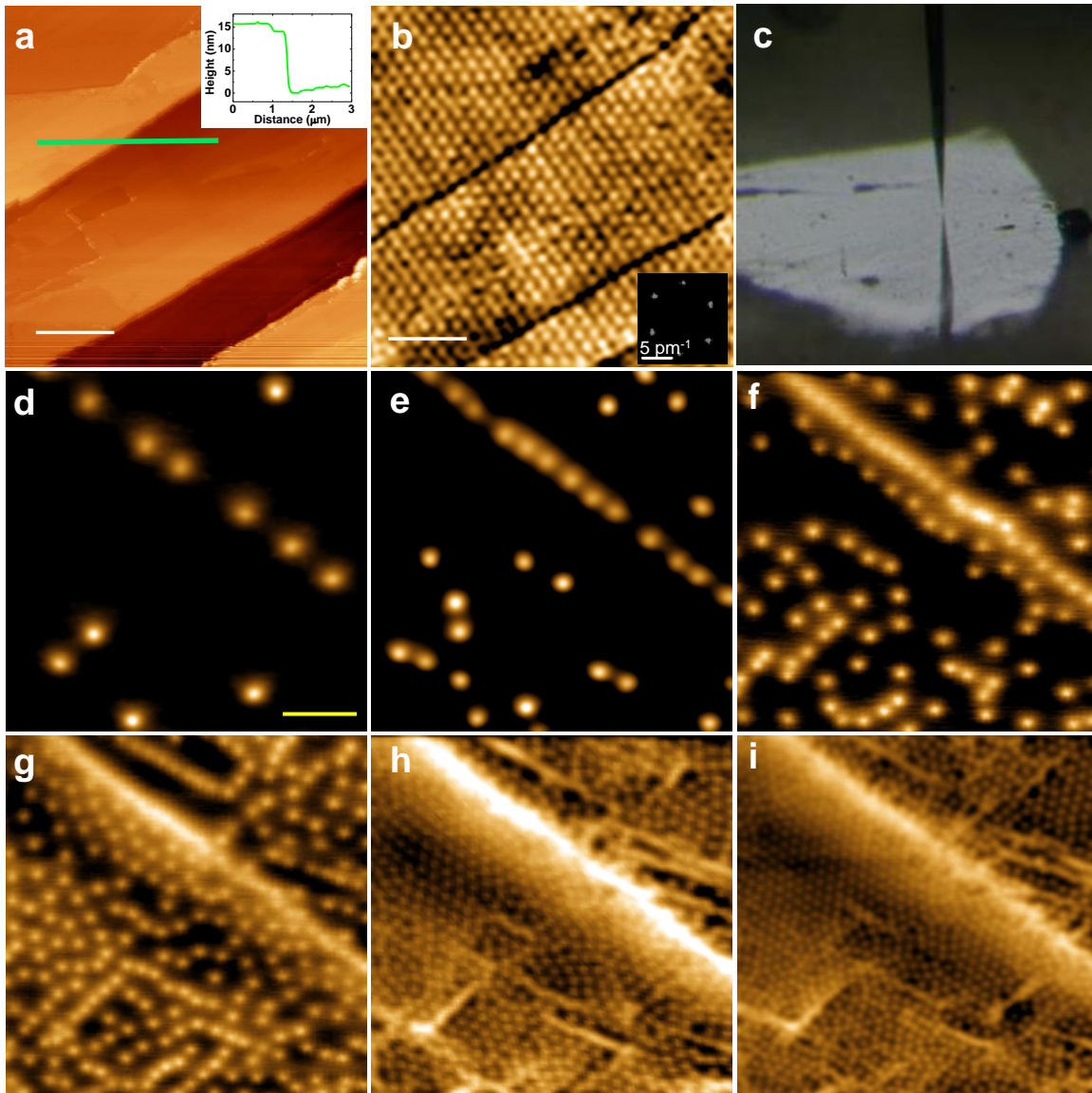


FIG. 1. **MFM and SOT imaging of the vortex lattice in β -Bi₂Pd.** **a** Typical topographic AFM image, with a line profile that show a 15 nm step in the inset (green line). **b** MFM image showing the vortex lattice at 2 K and 300 Oe and its Fourier transform (inset). The vortex lattice is clearly hexagonal over the whole area. The color code represent the shift of the resonance frequency of the cantilever where white denotes the normal phase and black the superconducting phase. Dark lines and other darker regions in the MFM image are the result of the non-magnetic tip-sample interaction. The scale bar in both images is of 1.4 μm . **c** Optical image of the SOT at a few tens of μm from the β -Bi₂Pd surface. The SOT reflection on the surface is visible on the bottom part. **d-i** $20 \times 20 \mu\text{m}^2$ SOT images that represent the out-of-plane field $B(x, y)$ obtained after field cooling the sample in magnetic fields of 2 **d**, 3 **e**, 6 **f**, 25 **g**, 35 **h** and 50 **i** Oe. The vortex gel is formed below about 20 Oe. The color scale represents with a span of 13 G **d-f**, 32 G **g** and 27 G **h-i**. The scale bar in **d** is for all SOT images and is 4 μm long.

posite occurs with $dT_c/dP < 0$. The pressure dependence of T_c in β -Bi₂Pd was measured in bulk samples^{30,31}, giving $dT_c/dP = -0.025$ K/kbar. $T_{c,bulk} = 5$ K for the unstressed region and our SOT measurements are per-

formed at $T = 4.2$ K. Thus, a variation in T_c of a fraction of a degree is sufficient to change penetration depth by a factor ~ 2 . Specifically if we consider that $\lambda(T) = \lambda(0)/\sqrt{1 - (T/T_c)^4}$, we estimate $T_{c,defect} = 4.38$

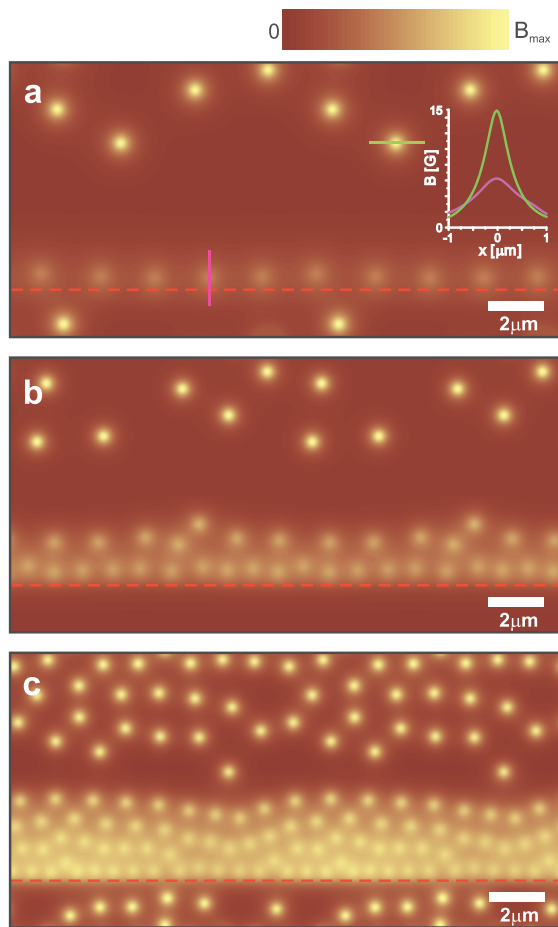


FIG. 2. **Simulation of vortex configurations close to a linear defect.** We show vortices as bright spots. To obtain vortex positions, we introduce a critical temperature variation as a function of the position from the defect Δx , taking $T_c(\Delta x) = T_{c,defect} + (T_{c,bulk} - T_{c,defect}) \frac{(\Delta x)^2}{L_D^2}$, where L_D is the lateral size of the defect. Note that we allow for a slow decay when leaving the linear defect. The position of the defect is marked by a red dashed line. Panels **a-c** show a field of view of $10 \times 20 \mu\text{m}^2$, for applied magnetic fields of 2 Oe, 5 Oe, and 15 Oe, respectively. We plot the magnetic induction at a height of 300 nm above the sample surface. This gives a span of ≈ 15 G (**a**), 16 G (**b**) and 18 G (**c**) in each image. Inset in **a** shows comparative magnetic profiles of two selected vortices, marked in the main panel by green and magenta lines.

K. According to the study of Ref. 30, this T_c corresponds to a local pressure of ~ 20 kbar. This subtle local change in T_c is very difficult to detect using other techniques, as we discuss in Supplementary Note 4.

To analyse further vortex distributions, we calculate the elastic energy associated to pairs of vortices, F , at different locations in our images. We compare the result for vortices located at a step with the elastic energy for pairs of vortices far from the steps. To this end, we use $F = \frac{\phi_0^2}{4\pi\mu_0\lambda^2} \log(\kappa) + \frac{\phi_0^2}{4\pi\mu_0\lambda^2} K_0(d/\lambda)$ for the free energy per unit length of two vortices interacting with each

other at a distance d^{32} . The first term comes from the energy of superfluid currents, giving the line tension of the vortex, and the second term denotes the interaction energy between vortices. K_0 is the order zero modified Bessel function of the second kind. We then calculate F for vortices far from defects using the bulk λ . For vortices at the steps we use λ measured close to defects. We find that the difference in free energy between the two situations is $\delta F \approx 7 \times 10^{-12} \text{ Jm}^{-1}$. This result is independent of the intervortex distance, for fields of order of a few tens of Oe or less. Below ≈ 50 Oe the intervortex distances vary from 0.5 to $4 \mu\text{m}$ and the second term of the interaction energy remains negligible with respect to the first term. Thus, at low magnetic fields, the intervortex interaction essentially vanishes and vortices behave as nearly isolated entities.

For fields above ≈ 50 Oe, the vortex lattice density increases and the previous two-vortex interaction approximation is no longer valid. We take into account the interaction with the first six neighbours arranged in a hexagonal lattice. We can use the same equation as before, but with an interaction term of $6 \times \frac{\phi_0^2}{4\pi\mu_0\lambda^2} K_0(a_0/\lambda)$. The difference in energy between six vortices close to a defect obtained using the two different values of λ considered here changes with the intervortex distance. We find that when vortices at the linear defect are closer than about 250 nm, it is no longer energetically favorable to add new vortices in there, so that linear defects saturate and a homogeneous vortex lattice is formed over the whole sample.

Thus, our direct imaging of the evolutionary patterns of superconducting vortex configurations in $\beta\text{-Bi}_2\text{Pd}$ in a broad range of magnetic fields shows that linear pinning centers produce a scaffold that cluster vortices along lines and leave large vortex free areas. At higher fields, when the intervortex distance is much smaller than the separation between defects, a triangular lattice forms within the vortex free areas observed at low magnetic fields.

Another striking insight from our measurements is that the standard deviation of the distribution of vortices diverges for very small vortex densities as the inverse of the square root of the magnetic field. The flux is quantized at each vortex, so that we can assume that $B = \frac{N}{A} \Phi_0$ within the fields of view studied here (N is the total amount of vortices and A the area) and in agreement with the magnetic field dependence of the intervortex distance following the triangular lattice expression (inset in Fig. 3b). In case of a purely one-dimensional row of vortices of length L , the average magnetic field along the row goes like $B \propto \frac{N}{L} \Phi_0$ and the intervortex distance diverges as $d_{1D} \propto \left(\frac{\Phi_0}{B}\right)$, which gives intervortex distances d_{1D} much smaller than a_0 if we consider vortex rows in two-dimensional areas. A scaffold of one-dimensional lines distributed within a two-dimensional area A presents a standard deviation of intervortex distances normalized by a_0 which increases when decreasing the magnetic field and diverges as $1/\sqrt{\mu_0 H}$, as we observe experimentally.

On the contrary, if we consider a homogeneous ran-

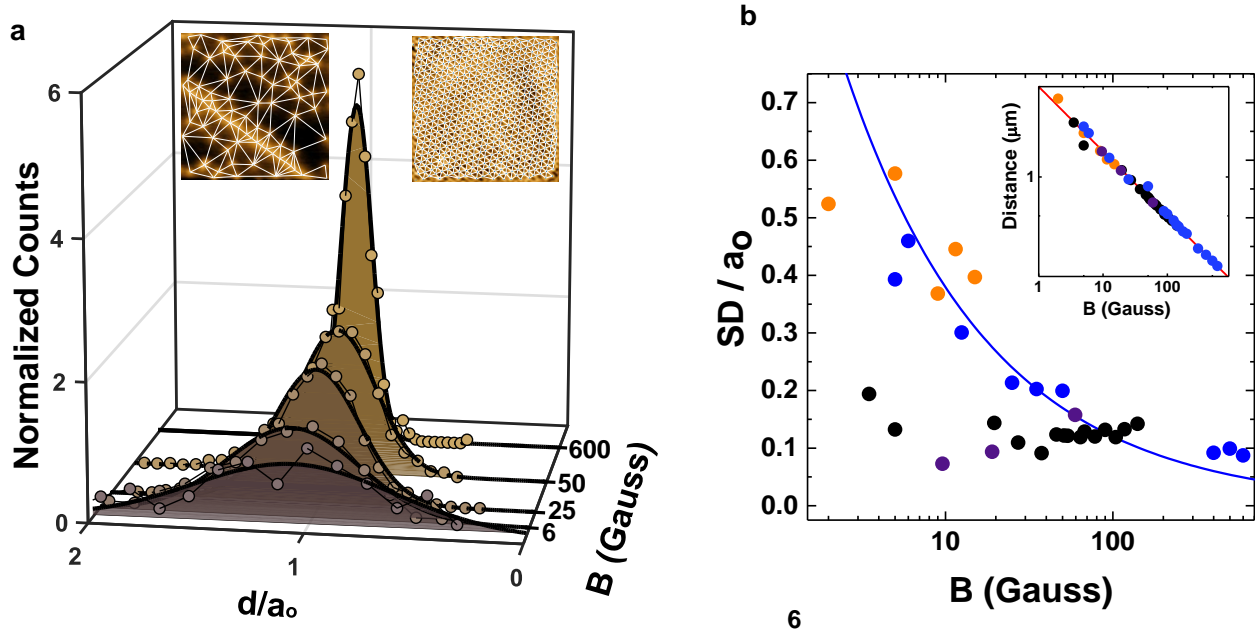


FIG. 3. **Intervortex distances and standard deviation.** **a** Histograms of the intervortex nearest neighbor distances for different magnetic fields normalized by the integrated area at 6 G, 25 G, 50 G and 600 G. In the insets we show SOT (left inset, image taken at 5 G) and MFM (right inset, image taken at 600 G) images, together with their Delaunay triangulation (white lines). **b** Standard deviation (SD) from histograms in **a**, normalized to the intervortex distance a_0 . Data from SOT and MFM are shown as blue dots. The simulations are shown as orange dots. Black points correspond to the data in the quasicrystalline Bragg glass phase nucleated in pristine cuprate samples and violet points to a disordered lattice in presence of columnar defects. The blue line is $1/\sqrt{\mu_0 H}$. In the inset we show intervortex distance vs the magnetic field for the same images.

dom distribution of point pinning centers, the vortices are pinned randomly. As the intervortex distance varies with the vortex density, the deviation of intervortex distances over the average value remains constant when decreasing the magnetic field. This explains the difference between the data in the vortex phases observed in cuprates and the divergence observed in β -Bi₂Pd in Fig. 3b. Actually, we can understand the behavior in β -Bi₂Pd as 1D dominated pinning at very low magnetic fields, which becomes usual 2D or 3D dominated pinning at higher magnetic fields.

In addition, the difference between the vortex distributions observed in β -Bi₂Pd and in the cuprates is that in the former there are strong spatial variations in the vortex density. Thus, there is a parallel with structural glasses and gels that is straightforward. In a similar way that gels are different from glasses because they are created from spatially highly inhomogeneous amorphous particle arrangements, the vortex gel differs from other vortex lattices, such as the Bose glass or the Bragg glass, by a highly inhomogeneous vortex distribution. There are multiple forms of gels and all share the presence of a scaffold that holds a network of particles. Accordingly, statistical properties of particle distribution and sizes are varied and mimic the properties of the scaffold. Here we have very simple particles, all equal to each other and characterized by carrying exactly a quan-

tized flux, whereas most gels are formed by polymers or other complex structures. The scaffold is also relatively simple, linear defects on a crystalline lattice. Therefore, the statistics of the vortex gel reveals the distribution of these linear defects in the sample.

Often, gels form self-similar or fractal structures. It has been shown that the fractal dimension remains constant with density, unless the density is significantly decreased, in which case the rugosity of constituents increases with decreasing density and the corresponding fractal dimension too³³. It is thus interesting to ask whether the distribution of vortices at low magnetic fields also shows similar features. We have calculated the generalized dimension D_q and the multifractal spectrum $f(\alpha)$ (details are provided in the Methods section). The results are shown in Fig. 4. Images showing triangular or disordered lattices provide distribution of fractal subsets centered at $\alpha = D_q = 2$. When we start observing strong variations in the vortex density, the lacunarity increases, which leads to $f(\alpha)$ that are much broader and whose maximum deviates from 2. D_q also increases for small values of the multiscaling exponent q . Thus, the vortex distributions at small magnetic fields are multifractal, with a probability of fractal subsets that strongly increases when decreasing the magnetic field, leading to a widening of $f(\alpha)$. On the other hand, the maximum of $f(\alpha)$ and the value of D_q for small q is larger than two

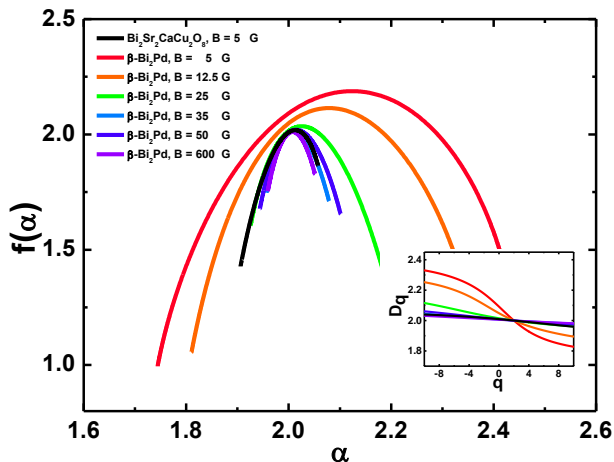


FIG. 4. **Multifractal analysis of the vortex images at very low magnetic fields.** We show in the main panel the distribution of fractal dimensions $f(\alpha)$ in a cuprate superconductor (black line) for 5 Oe and in β -Bi₂Pd (rest of colored lines) for different magnetic fields from 5 Oe to 600 Oe. For the cuprate superconductor, larger images or images at other magnetic fields lead to curves with much smaller dispersion of α , centered at $\alpha = 2$. In the inset we show the generalized dimension D_q as a function of the set of exponents q . Note that the curves strongly vary for low magnetic fields, but remain centered around 2 for high magnetic fields and for the results in the cuprate superconductor.

and increases when the magnetic field is decreased. Such a behavior occurs for example in pictures of crumbled paper, as opposed to systems with no lacunarity. Linear features and voids in between lines provide fractal subsets whose probability can be larger than two and have been observed in galaxy and dark matter distributions³⁴.

The outstanding feature of the vortex gel is that the standard deviation of vortex positions diverges for decreasing magnetic fields, suggesting that the magnetic field penetration is neither a Meissner state interspersed with normal areas (the intermediate state⁷), nor an intermediate mixed state with hexagonal vortex clusters (as in pure Nb^{16,35}), nor the disordered vortex phases observed in high T_c cuprate superconductors^{1,2} (more details about these phenomena are provided in Supplementary Note 5). Other arrangements with strong variations in vortex densities are found in conformal crystal arrays of pinning centers and when periodic and random pinning potentials are formed³⁶⁻³⁸. In the latter case simulations show that the presence of square crystal and hexagonal vortex lattices can lead to one-dimensional fractal structures, in a small range somewhat below the pinning strength range where the combination of random pinning and the crystal lattice is sufficiently strong to form vortex chains³⁶. Our work shows that this actually occurs in a wide range of magnetic fields in presence of one-dimensional pinning centers, leading to vortex dis-

tributions with structural properties typical of a gel.

Vortex positions are determined by pinning, and we do not see indications of thermal fluctuations playing a role in the vortex location (see Supplementary Notes 4 and 6). Thus, the transition from the normal phase into the vortex liquid (which can only appear in an extremely small temperature range in β -Bi₂Pd) and the vortex gel should be continuous and be produced by dynamical arrest. Thus, it depends rather on the diffusion process of vortices along the pinning centers than on equilibrium properties of the superconductor. As such, it should appear in all superconductors with a small amount of fluctuations and pinning centers with a spatially inhomogeneous distribution.

CONCLUSIONS AND OUTLOOK

Our measurements illuminate the interplay of geometric defects and crystalline stress at very low magnetic fields in superconductors, which turns out to be much more varied than previously thought. We reveal a novel vortex gel phase, governed by organizing principles that combine pinning centers as scaffolds and ever present Meissner screening that promotes large voids in the vortex lattice.

Screening has been considered to design mechanical resonators that are isolated from the environment for quantum circuits, to produce a scaffold of traps for cold atoms close to the surface of a superconductor or to design magnetic cloaks³⁹⁻⁴¹. Such designs remain however very difficult to realize in dense vortex lattices at high magnetic fields. By contrast, the vortex gel state produces intrinsically areas with flux expulsion and flux concentration allowing to engineer with unprecedented spatial control the local magnetic field. Furthermore, the regions with clusters can provide a platform to manipulate and entangle vortices. Recent work shows that Majorana modes might be present in superconducting vortices⁴². This calls for methods to manipulate vortices and entangle their states to search for non-Abelian statistics^{43,44}. Superconductors considered are, among others, Fe based materials whose structural properties and superconducting parameters are similar to β -Bi₂Pd⁴⁴⁻⁴⁶. Our results show that vortices are nearly independent to each other at very low magnetic fields. This suggests that vortices in this field range are also highly manipulable, much more than in usual hexagonal or disordered vortex lattices.

ACKNOWLEDGMENTS

We acknowledge support, discussions and critical reading of the manuscript from Eli Zeldov, who also devised and set-up the SOT system. We also acknowledge critical reading and suggestions of Vladimir Kogan.

I. METHODS

Sample preparation

β -Bi₂Pd single crystals were grown as described in Ref. 18. The β -Bi₂Pd phase is thermodynamically unstable at room temperature. Crystals need to be quenched from the high temperature β -Bi₂Pd phase by immersion in cold water. Structural characterization gives high quality single crystalline samples. The superconducting transition ($T_c = 5$ K) is sharp in all thermodynamic measurements^{17,19}. However, the residual resistivity, of $18 \mu\Omega\text{cm}$ is quite high, pointing out that, during the quench, a sizeable amount of defects has been left in the sample. The electronic mean free path is of $\ell \approx 15$ nm (from residual resistivity¹⁸) and the thickness of the sample is of about 0.1 mm.

We prepare the sample surface by cleaving with scotch tape and obtain atomically flat surfaces suitable for scanning probe imaging. In the Supplementary Note 1, we provide a detailed analysis of the sample surface, including the formation of twist hackles and other defects during fracture when cleaving. The magnetic field is applied perpendicular to the surface using superconducting coils. The plate like single crystals used here give demagnetizing factors close to one and we usually measure in field-cooled conditions, heating the sample above T_c after each field change.

Magnetic Force Microscopy

Magnetic force microscopy (MFM) measurements have been performed in a commercial Low-Temperature SPM equipment from Nanomagnetics Instruments, working in the 300 K - 1.8 K temperature range. The microscope is inserted in a superconducting coil⁴⁷. Simultaneous atomic force microscopy (AFM) and magnetic MFM images are obtained in dynamic mode, oscillating the cantilever at its resonance frequency, and using the so-called retrace mode for magnetic detection. In this mode, the tip scans twice over the sample surface at two different distances. A first scan is performed at distances of few nm to extract the AFM profile. Then, the tip is retracted by a selected distance (~ 100 nm in this work) and the system repeats the same profile obtained in the first scan. Phase shift of the cantilever oscillation during this retrace scan, caused by the long range magnetostatic interaction, is used to build the MFM image. We use commercial MFM tips from Nanosensors (PPP-MFMR) and magnetize these prior to the measurement by applying a magnetic field of 1500 Oe at 10 K. We discuss aspects of magnetic contrast as obtained with the MFM in Supplementary Note 4.

Scanning SQUID-on-tip Microscopy

Scanning microscopy with a SQUID-on-a-tip (SOT) images provides high spatial resolution magnetic imaging^{48,49} reaching single-spin sensitivity^{20,21} and enabling detection of sub-nanometer and ultrafast vortex displacements^{50,51}. The SOT used in this work had an effective diameter of 260 nm, 160 μA critical current and white flux noise of around $800 \text{ n}\Phi_0 \text{ Hz}^{-1/2}$ above a few hundred Hz. The SOT was mounted in a home-built scanning probe microscope with a scanning range of $30 \times 30 \mu\text{m}^2$ and read out using a series SQUID array amplifier⁵². The SOT images in this manuscript show an area of $20 \times 20 \mu\text{m}^2$ with a pixel size of $100 \times 100 \text{ nm}^2$. The acquisition time was 100 s per image. All measurements were performed at 4.2 K in an open loop mode, at constant height of ~ 300 nm above the sample.

Ginzburg-Landau numerical simulations

The numerical simulations were performed within the Ginzburg-Landau (GL) formalism, taking into account the spatially inhomogeneous microscopic parameters. In their stationary form, the dimensionless GL equations for the superconducting order parameter Ψ and the magnetic vector potential \mathbf{A} read:

$$(-i\nabla - \mathbf{A})^2\Psi = (f(\mathbf{r}) - g(\mathbf{r})|\Psi|^2)\Psi, \quad (1)$$

$$-\kappa(0)^2\nabla \times \nabla \times \mathbf{A} = \text{Im}(\Psi^*\nabla\Psi) - |\Psi|^2\mathbf{A}, \quad (2)$$

where $f(\mathbf{r}) = \frac{1-t(\mathbf{r})^2}{1+t(\mathbf{r})^2}$ and $g(\mathbf{r}) = \frac{1}{(1+t(\mathbf{r})^2)^2}$ contain the temperature dependence (proposed empirically in Ref. 53, and proven to describe well the standard experimental observations) and the spatially-dependent critical temperature through $t(\mathbf{r}) = T/T_c(\mathbf{r})$. In Eqs. (1-2), $\kappa(0) = \lambda(0)/\xi(0)$ is the GL parameter at zero temperature, the distance is measured in units of the coherence length $\xi(0)$, the vector potential \vec{A} in $\hbar/2e\xi(0)$, and the order parameter Ψ is scaled to its value at zero field and temperature. We apply a finite-difference representation for the order parameter and the vector potential on a uniform 2D (x,y) Cartesian space grid, with spatial resolution of $0.1\xi(0)$. We use periodic boundary conditions on the simulated rectangular cell $W_x \times W_y$, in the form $\mathbf{A}(\mathbf{r} + \mathbf{b}_i) = \mathbf{A}(\mathbf{r}) + \nabla\eta_i(\mathbf{r})$, and $\Psi(\mathbf{r} + \mathbf{b}_i) = \Psi \exp(2\pi i\eta_i(\mathbf{r})/\Phi_0)$, where $\mathbf{b}_{i=x,y}$ are the supercell lattice vectors, and η_i is the gauge potential. Since the sample is exposed to a homogeneous perpendicular magnetic field $\mathbf{H} = H\mathbf{e}_z$) we employ the Landau gauge $\mathbf{A}_{ext} = Hx\mathbf{e}_y$ for the external vector potential and $\eta_x = HW_x y$ while $\eta_y = 0$. The value of applied magnetic field must always match the integer number of flux quanta (vortices) in the simulated cell, as stipulated by the virial theorem⁵⁴. In most simulations we deliberately choose $W_x = \sqrt{3}W_y$ that should favor a periodic triangular lattice of vortices, so that every departure from an Abrikosov lattice pattern is easily seen.

Analysis of images

To obtain the multifractal properties of the images, we first identify vortex positions and create a binary image with vortex positions. We then run a program available in Ref.⁵⁵. We start by a box counting algorithm to find the number of pixels for different counting box sizes, ϵ , and we calculate the probability $P_{i\epsilon}$ of having pixels in each box. We then define arbitrary exponents, q to describe how the pixel distribution scales with ϵ and calculate $I_{q\epsilon} = \sum_{i=1}^N (P_{i\epsilon}^q)$ and $\mu_{qi\epsilon} = \frac{P_{i\epsilon}^q}{I_{q\epsilon}}$ to obtain $A_{q\epsilon} = \sum_{i=1}^N (\mu_{qi\epsilon} P_{i\epsilon})$. The slope of $A_{q\epsilon}$ vs q in a log-log plot gives α . By fitting $\tau_{q\epsilon} = \frac{\sum_{i=1}^N (P_{i\epsilon}^{q-1})}{N}$ as a function of ϵ in a log-log plot we obtain τ_q . We can then obtain the multifractal spectra $f(\alpha)$ using $\tau_q = \alpha q - f(\alpha)$. D_q is given by $D_q = \frac{\tau_q}{q-1}$.

AUTHOR CONTRIBUTIONS

LE and YA performed the SOT experiment and AC, JAz, FM, MGH and CM performed the MFM measurements, receiving input from IG and HS. RL, JA and EH synthesized the crystal. Images were analyzed jointly by AC, CM (MFM) and YA (SOT), with input from IG and HS. JA and YF provided images in cuprates. JB performed the standard deviation and fractal analysis. JDG and MVM performed the GL simulation and analyzed the data. The discussion of the interpretation was made by IG, YF, HS and YA with contributions from all authors. YA and HS wrote the paper with contribution from all the authors.

SUPPLEMENTARY NOTE 1: FRACTOGRAPHIC ANALYSIS OF CLEAVED SURFACES OF β -Bi₂Pd

The bonds in the tetragonal structure of β -Bi₂Pd are such that the surface is most likely formed by the square lattice of Bi atoms⁵⁶. The cleaving plane is thus very well defined and lies perpendicular to the c-axis. There are no indications from van der Waals like bonds as in transition metal dichalcogenides—this material has well established three-dimensional electronic properties⁵⁷. Nevertheless, it is a fact that it can be easily cleaved using scotch tape^{18,19,58,59}. Cleavage occurs without any residues, as thick sheets of the material are removed when cleaving. The obtained surface is shown in a optical and scanning electron microscope (SEM) images in the Supplementary Figure 5. The surface is very shiny and has features which are important for the results discussed in the main text.

Cleaving or breaking of a surface occurs through the establishment of a fracture or crack at a few places close to the edges of the sample. The fracture then propagates as a crack front through the whole sample. The action on the sample during fracture consists of tear, shear and compressive forces (called mode I, II and III fracture, respectively, see Supplementary Figure 5a)⁶⁰⁻⁶². If the action would occur only along the c-axis, just tear forces that separate layers would be active. However, the competition between elastic energy and surface energy is in-plane anisotropic, leading to crack behavior that depends on the in-plane properties of the material. This occurs irrespective of the anisotropy of the in-plane vs out-of-plane crystalline structure, and is even observed in two-dimensional van der Waals materials⁶³. In three-dimensional crystals this issue is even more important. The sample is of course not perfect and the crack front encounters defects such as small angle grain boundaries^{64,65}. In a cleaving process using scotch tape, shear forces appear even more easily than cleaving with a knife, because scotch is highly deformable. Shear forces change the direction of crack propagation away from high symmetry crystalline lines. In addition, fracture produces a release of stress that might have been left over during crystal growth (for example by the presence of small temperature gradients). The process of releasing this load is influenced by defects and imperfections in the crystal. All this leads to regions with alternating compressive and tensile stress and causes a twist action (combining shear and tear, modes II and III in Supplementary Figure 5a) that might well propagate far below the surface and influence large areas of the crystal⁶⁰.

The features produced by this twist action are called twist hackles and must not necessarily follow a crystalline direction. They rather correspond to steps that run parallel to the crack propagation direction. In β -Bi₂Pd we observe features that can be associated to twist hackles. We mark a few of such features by yellow dashed lines in the Supplementary Figure 5b-d. Close to the sample edges, twist hackles have a strong tendency to start or arrive to the end of the sample at an angle to the surface, following the crack propagation direction, as we observe in the images (Supplementary Figure 5d).

However, the crack propagation direction is certainly influenced by the direction of the crystalline axis. Thus, there are also a number of linear structures at 45 or so degrees to the twist hackles that can be associated to crystalline axes (we mark a few by red dashed lines in the Supplementary Figure 5b,e). There are furthermore linear features perpendicular to all them. Thus, the surface is composed of features resulting from twisting efforts produced during fracture that might influence the whole sample. The macroscopic twist is compensated by an arrangement of linear features at right angles or at 45 degrees to each other.

Let us note that we also identify large wrinkles on the surface (red arrows in Supplementary Figure 5 b). The wrinkles appear close to very large defects (broken or open features in the Supplementary Figure 5 a). A closer analysis using scanning electron microscopy (SEM) reveals a large number of separated layers close to wrinkles (Supplementary Figure 5g). Generally, step edges appear strongly marked in SEM images (Supplementary Figure 5f-h), suggesting that there is a separation of parts of the sample (green arrows in Supplementary Figure 5g-h). All this supports the presence of large twisting effort during fracture.

Our experiments are made close to the center of the sample, in locations showing no large wrinkles and the tip was carefully positioned away from optically visible defects. So that we are far from wrinkles produced during cleaving (red arrows, Supplementary Figure 5 b). However, the linear structures we observe in the images are certainly due to twist hackles that are all over the sample. Close to twist hackles, there is enough strain to modify the local superconducting properties, as observed in the SOT experiments.

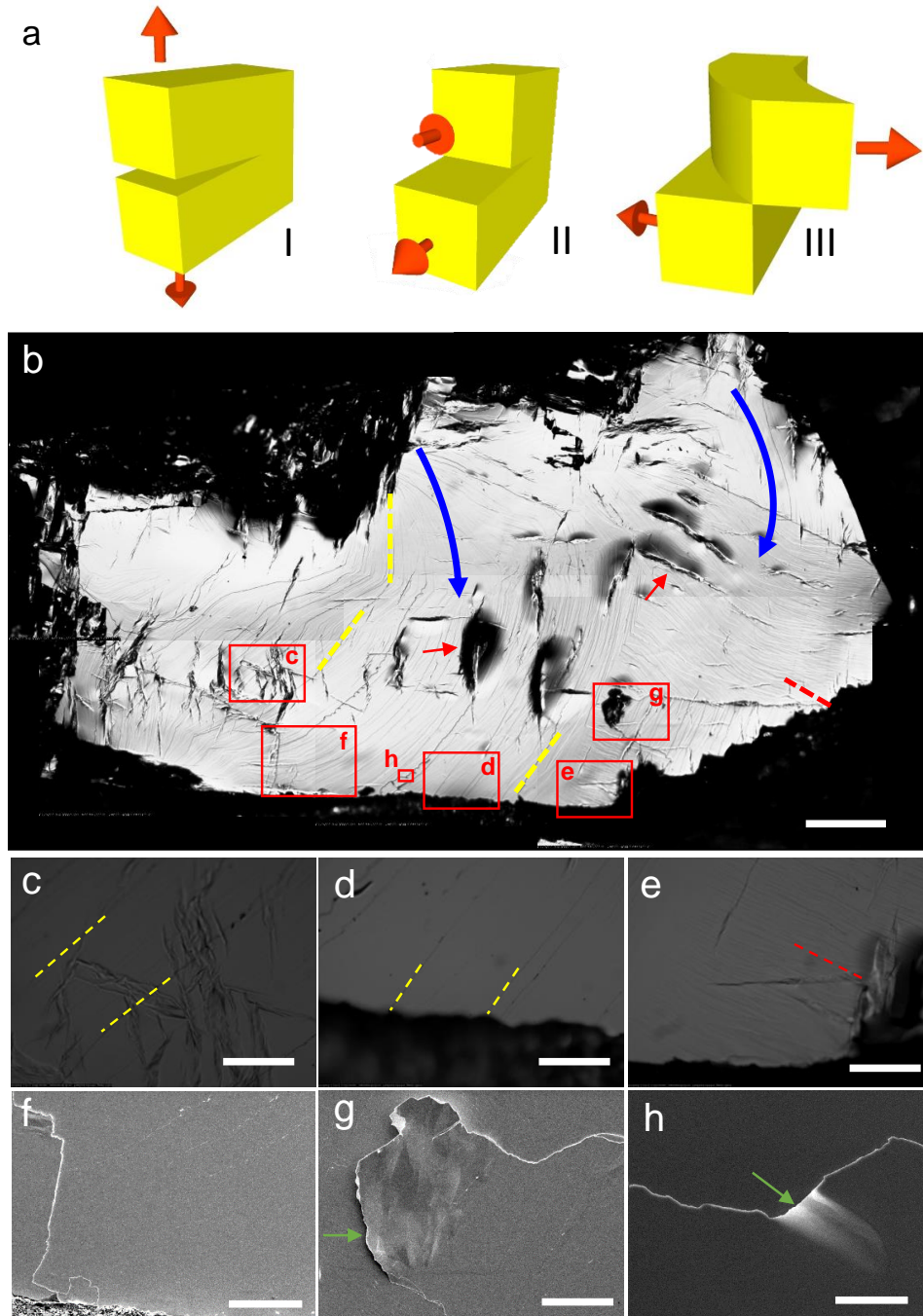


FIG. 5. **Optical and SEM analysis of fractured surfaces in β -Bi₂Pd.** **a** Forces exerted during the cleavage process of a single crystal. In the opening mode (mode I) there is tensile stress normal to the plane of the crack. The sliding mode (mode II) describes shear stress parallel to the plane of the crack and perpendicular to the crack front. The tearing mode (mode III) a shear stress parallel to the plane of the crack and parallel to the crack front. **b** Optical picture of a sample after cleaving. We identify twist hackles (yellow dashed lines), linear features that seem step edges along crystalline directions (red dashed lines) and the debonding path, or the direction where the crack front propagated during fracture (blue lines). **c-e** Magnified areas marked by red rectangles in **b** taken using an optical camera. **f-h** SEM images. We mark places where the sample forms fully detached layers by green arrows. Images are at the red rectangles shown in **b** marked by the corresponding letters (f, g and h). Scale bars are of 0.2 mm in **b**, 40 μm in **c**, **d** **e** and **g**, 50 μm in **f** and 8 μm in **h**.

**SUPPLEMENTARY NOTE 2: TOPOLOGICALLY NON-TRIVIAL PROPERTIES OF THE
BANDSTRUCTURE**

Measurements of angular resolved photoemission in the normal phase above T_c suggest non-trivial topological behavior at the surface of β -Bi₂Pd^{58,59}. The band-structure observed by photoemission coincides with calculations and has mixed contributions from Pd $4d$ and Bi $6p$ orbitals that give three main sheets of convolved geometries that partially overlap with each other^{66,67}. Photoemission reveals a Dirac cone well below the Fermi level⁵⁸. Spin resolved measurements provide polarized bands close to the Dirac cone. The same authors suggest that topologically non-trivial spin polarized bands crossing the Fermi level might rise up to the surface. The STM experiment of Ref. 59 provides indications for a small triplet component appearing at the surface. In another STM experiment on epitaxially grown thin films, authors found superconducting properties that are different from the bulk behavior⁶⁸—the critical temperature was somewhat larger and two gaps were detected in the tunneling conductance. Furthermore, a zero-bias peak appears in the center of the vortex cores, indicating the formation of vortex bound states^{69–71}. Authors argue that these states could be topologically non-trivial, contrasting earlier results found in other superconducting materials. A recent report shows non-integer flux quantization in rings made of thin films of Bi₂Pd, suggesting the formation of a π junction that authors associate with unconventional superconducting properties⁷². Our results provide new insight in this debate. The flux carried by single vortices can vary with respect to the flux quantum Φ_0 in topological superconductors, due to enhanced stability of fractional vortices⁷³. The observation of vortices with a weaker magnetic field profile as the ones located on a defect in our case could be explained by their flux below Φ_0 , instead of a varying penetration depth. However, the change in λ describes our results significantly better (see Supplementary Note 3). Let us also remark that fractional flux quantization can also occur in long Josephson $0 - \pi$ junctions, where the phase difference varies along the junction^{74,75}. Such junctions can form in superconductors with anisotropic gap structures or ferromagnetic inclusions. It is not clear how such a situation can be formed close to a linear defect in β -Bi₂Pd and lead to the observed increase in λ . Thus, we can conclude that, at present, we have no evidence for topologically non-trivial behavior from our experiments.

SUPPLEMENTARY NOTE 3: FITTING PROCEDURE OF SOT SCANS

There are two unknown parameters that are essential to obtain a meaningful fit to a magnetic field profile obtained with SOT.

One is the distance between the sample and the SOT d_{SOT} and the other is the SOT transfer function that converts the measured current that flows in the SOT into a magnetic field (dI_{SOT}/dB). The latter is determined precisely by measuring the response of the SOT to a known applied magnetic field. Here, the presence of the superconducting sample partially screens the applied field. It is therefore somewhat hard to know which part of the applied field is screened by the sample. We thus assume that vortices far from defects, those that appear brightest in the images, have a flux of Φ_0 and $\lambda = 186 \text{ nm}$ ¹⁹.

Then, we model the field $B(x, y)$ by a monopole located at λ below the surface i.e. at a distance $\lambda + d_{SOT}$ from the sample. All vortices far from the defects that appear bright in Figures 1 d-e are fitted with fitting parameters d_{SOT} and dI_{SOT}/dB . Averaging results in different vortices we find that $d_{SOT} = 270 \text{ nm}$. We also obtain the magnetic field scale in the images by obtaining dI_{SOT}/dB . We considered in 9 bright and 10 less pronounced vortices from Figs. 1 d-e.

Let us now discuss two representative examples for vortices, one showing bright spot and another one a less pronounced spot in the SOT images. The magnetic field profile $B(r)$ across each vortex is shown in the Supplementary Figure 2, together with two different fits.

We first assumed that the flux is smaller for a vortex located at a defect. To model this situation a fixed $\lambda = 186 \text{ nm}$ is considered while the magnetic flux is left as a free parameter. The results are shown in Supplementary Figure 6a. Bright vortices are well described by that value of λ and a value for the flux obtained from the fit very close to the flux quantum, at $1.06\Phi_0$. The vortex on the defect yields however a smaller flux, $0.62\Phi_0$.

As a second hypothesis, we considered Φ_0 is the same for all vortices and that λ differs at different locations. The results are shown in Supplementary Figure 6b. Here, vortices far from defect yield 172 nm for λ , which is very close to the reported value¹⁹. The vortex close to the defect yields $360 \sim \lambda_D$. The values of λ stated in the main text are obtained by averaging the results over different vortices. This second hypothesis, leading to a constant Φ_0 is much more consistent with expectations for simple s-wave superconductivity and, in addition, the quality of the fits is considerably improved with respect to the other option.

We thus conclude that λ is not homogeneous over the sample and is modified, particularly at twist hackles and other linear features that are found in $\beta\text{-Bi}_2\text{Pd}$.

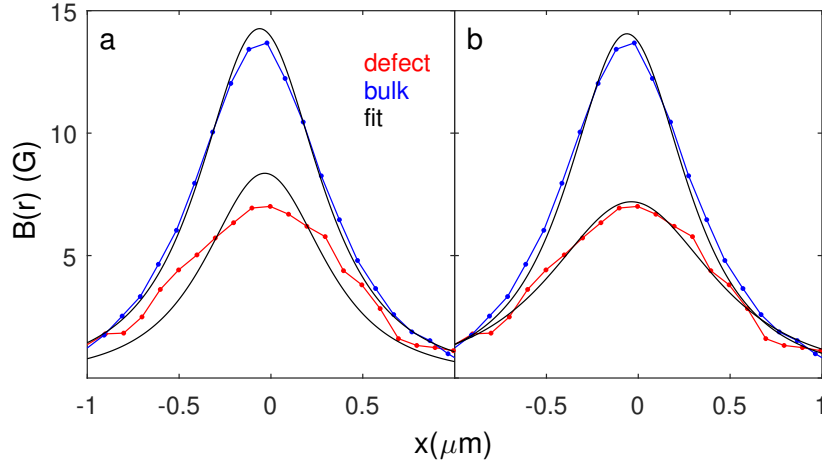


FIG. 6. **Field profiles obtained from SOT and fits showing the positional variation of λ .** **a,b** Vortex field profiles $B_z(r)$ along vortices far from a defect (blue) and close to a defect (red). Profiles taken from Figure 1d,e. **a** Fit of the vortex profile in black with free parameter the magnetic flux ϕ . Vortices far from defects provide an excellent fit with $1.06 \Phi_0$ where Φ_0 is the flux quantum. However, to fit the vortices at defects, we need to considerably reduce Φ down to $0.62 \Phi_0$. **b** Fit of the same vortex profiles, but using the penetration depth λ as a free parameter. Then, we can fit all vortices. Note that the quality of the fit is significantly better than in **a**. We find $\lambda = 172 \text{ nm}$ (which is of order of $\sim \lambda$ measured using Hall probes, as discussed in the main article) for vortices far from a defect and $\lambda = 360 \text{ nm}$ close to the average value found for vortices at a defect.

SUPPLEMENTARY NOTE 4: TEMPERATURE DEPENDENCE OF THE MFM IMAGES

The evolution of the flux line lattice with increasing temperature is shown in Supplementary Figure 7. In the MFM experiment, we observe the hexagonal vortex lattice up to temperatures of 4.5 K at a magnetic fields of 300 Oe. We mostly observe defect free vortex lattices and see no particular increase in the defect structure of the vortex lattice when increasing temperature. In Supplementary Figure 7a there are a few defects in the vortex lattice (vortices showing seven or five nearest neighbors). These are washed out when increasing temperature (Supplementary Figures 7b,c). Thus, the range of vortex liquid must be very small in β -Bi₂Pd.

The diagonal line located at the bottom of the image and visible at all temperatures is probably caused by a crosstalk between charging effects and the magnetic signal due close to a large step. The crosstalk between the two signals should not be temperature dependent and therefore we expect this feature to be magnetic. It might be indeed associated to a decrease in T_c along this line. The crosstalk makes it very difficult to make any quantitative estimation of T_c close to the step. On the other hand, the image taken at the highest temperatures (Supplementary Figure 3b and c) show a whitish vertical line highlighted by a black arrow. That line is absent in other images as shown in Figure 3a and might result from a change in T_c along this line. Again, with our present resolution in MFM, SOT and available STM experiments^{18,19} we cannot be more quantitative. MFM is probably influenced by the mentioned charging artifacts, SOT suffers from problems with temperature control and the estimated change in T_c corresponds to a change in the gap size of $50 \mu\text{V}$ which is impossible to detect in STM measurements taking into account the small but finite gap distribution close to $50 \mu\text{V}$ found in this compound^{18,59}.

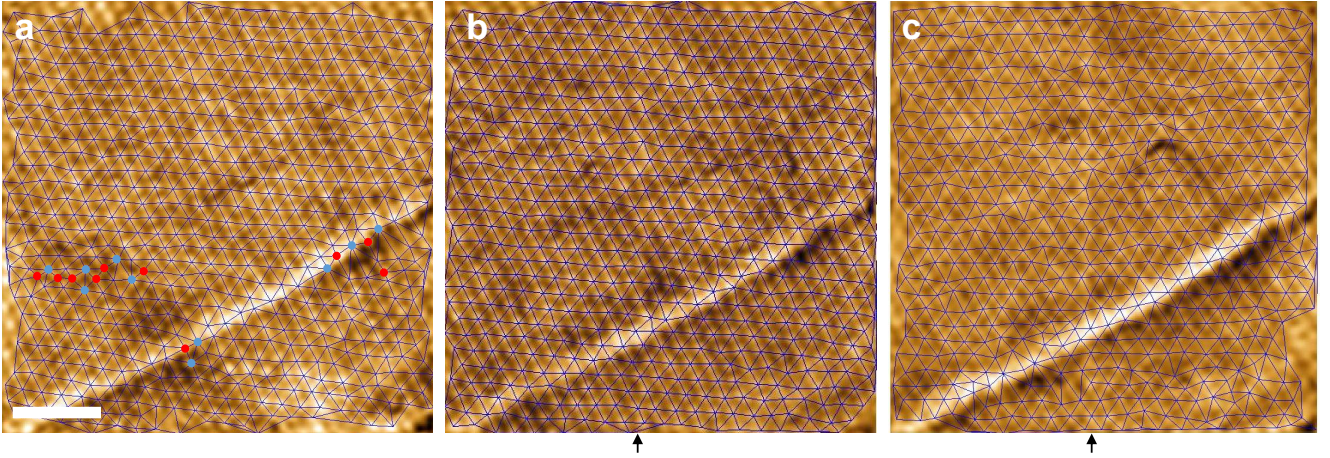


FIG. 7. Behavior of the hexagonal vortex lattice as a function of temperature measured with MFM . a-c images taken at 2.75 K, 3.75 K and 4.5 K, respectively at 300 Oe. The color scale represents the observed frequency shift. Scale bar is $1 \mu\text{m}$. Blue lines are the Delaunay triangulation of vortex positions. Blue and red points highlights vortices with seven and five nearest neighbors respectively. The dark arrow at the bottom highlights the position of the vertical line

SUPPLEMENTARY NOTE 5: MECHANISMS PRODUCING VORTEX CLUSTERING: JOSEPHSON BEHAVIOR AT LINEAR DEFECTS, TWO-GAP SUPERCONDUCTIVITY AND THE INTERMEDIATE MIXED STATE

A possible alternative explanation for vortex clustering along lines is that a Josephson-like junction forms step edges with strong pinning and deformation of Abrikosov-Josephson vortices^{76,77} along such a junction. But the existing low-temperature STM scans of characteristic step edges in β -Bi₂Pd do not show evidence of such junctions. It has been also shown that vortex-free regions, called Meissner belts, can appear close to large steps as a result of the Meissner current circulating near steps at the surface^{45,46}. At the same time, the presence of the steps also imposes boundary conditions on the vortex current which result in an attractive force toward the step edge. The result of these two forces could contribute to some extent to our observations.

We also recall the discussions of possible two-gap superconductivity in β -Bi₂Pd⁶⁸ and that vortex clustering, stripes and vortex free areas at low magnetic fields have all been observed in the archetypal two-gap superconductor MgB₂^{8,9,15}. There, two characteristic distances in the vortex pattern have been reported, with two peaks in the histogram of nearest neighbor vortex distributions. One which is called an intergroup distance and follows a_0 when varying the magnetic field and an intragroup distance that remains almost constant with respect to the applied magnetic field. It has been argued that the vortex stripes are independent of the crystal lattice and therefore cannot be related to strong pinning. Authors of Refs. 6, 8, 9, and 15 relate instead their findings to the magnetic competition of two coexisting gap-condensates in superconducting MgB₂. The vortex patterns we report here for β -Bi₂Pd are different. At very low fields, the patterns do contain vortex stripes, clusters and vortex free regions. However, the intervortex distances do not cluster around two values as seen in MgB₂. Instead, vortices arrange in lines along crystalline defects. As convincingly shown in Refs. 18, 19, and 78, β -Bi₂Pd is probably a single-gap superconductor, so vortex clustering cannot be associated to the hybridization of multiple gaps.

Vortex clustering has been seen in single-gap superconductors as well, with $\kappa \gtrsim \sqrt{\frac{1}{2}}$. The intermediate mixed state consists of clusters of vortices with widely differing intervortex distances that are often smaller than $d_{Abrikosov}$. Vortex lattices at fields close to or below H_{c1} imaged using magnetic decoration, scanning Hall-probe microscopy, and/or studied using small-angle neutron scattering often show a mixed intermediate state characterized by strong magnetic field gradients inside the sample, due to flux-free areas coexisting with areas having vortices inside^{1,14,79–83}. In high quality single crystals, such as e.g. Nb with $\kappa = 1.1\sqrt{\frac{1}{2}}$, flux-free regions coexist with domains of vortex lattice¹⁴, where the shape of domains resembles the intermediate state found in type I superconductors⁷. Small-angle neutron scattering finds the intervortex distance inside those domains exactly as expected at H_{c1} ^{16,35}. In our experiments, the magnetic flux integrated over large areas provides a magnetic induction of the same order in presence of an ordered vortex lattice and in presence of strong vortex clustering. Vortices are nucleated in the sample during the field-cooled procedure, and remain pinned even at very low magnetic fields, in spite of the strong field gradients produced when cooling below $H_{c1}(T)$. Such a feature has never been previously reported, to our knowledge, at low magnetic fields and in presence of strongly inhomogeneous vortex distributions.

SUPPLEMENTARY NOTE 6: FLUCTUATIONS VS PINNING

The elastic displacement of vortices $u(0)$ caused by a pinning force F depends on the magnetic field and temperature following $u(0) \approx F(\frac{4\pi}{B\Phi_0})^{1/2}\mu_0\frac{\lambda^2}{(1-\frac{B}{B_{c2}})^{3/2}} \approx F(\frac{4\pi}{B\Phi_0})^{1/2}\mu_0\frac{\Phi_0\ln\kappa}{B_{c1}(1-\frac{B}{B_{c2}})^{3/2}}$, for an isotropic superconductor with penetration depth λ (μ_0 is the magnetic permeability)^{1,2,84}. Close to steps, the increased λ thus yields an increased displacement of vortices $u(0)$. In addition, $B_{c1} \approx \frac{\Phi_0}{4\pi\lambda^2}(\ln\kappa + 0.5)$ is decreased, whereas $B_{c2} = \frac{\Phi_0}{\pi\xi^2}$ remains similar, provided that ξ is limited by the mean free path in the dirty limit regime.

Vortices suffer positional changes due to thermal activation, which can be discussed using elastic theory of the vortex lattice^{1,2,85}. The changes in the position are related to the temperature following $\langle u^2 \rangle \approx d_0^2(\frac{3GLB}{\pi^2 B_{c2}(0)})^{1/2}\frac{T}{T_c}\frac{\lambda^2(T)}{\lambda^2(0)}((1 - B/B_{c2})^3\ln(2 + \frac{1}{\sqrt{2B/B_{c2}}}))^{-1/2}$ (a_0 is the Abrikosov intervortex distance and GL the Levanyuk-Ginzburg number)^{1,2,86-89}. The fluctuation range is very small, because in any event GL is small in a conventional superconductor such as β -Bi₂Pd. Anisotropy enhances fluctuations but there is practically no anisotropy in β -Bi₂Pd^{18,19}. However, fluctuations are enhanced for large wavelengths, by taking into account nonlocal elastic interactions, and in presence of pinning induced disorder due to the mobility of dislocations and defects of the flux lattice^{85,90-93}. Vortex nucleation occurs here very close to the zero field T_c for very low magnetic fields, which would suggest that fluctuations might play a role.

Vortex entry occurs through thermal diffusion for long wavelengths $k^{1,2}$. There are two processes of vortex diffusion, giving an exponential decay $\exp(-\Gamma_1 t)$ with rates Γ_1 and Γ_2 ^{1,94}. First, through the lattice compression, giving $\exp(-\Gamma_1 t)$ with $\Gamma_1 \approx \frac{B}{\mu_0 B_{c2}}\rho_N k^2$ with ρ_N being the normal state resistivity. For very low magnetic fields of a few Gauss, and taking $\rho_N \approx 10^{-6}\Omega m$, we find $\Gamma_1 \approx 310^2 L^2$ in s, with L the wavelength in meters. Even for relatively long wavelengths of order of the sample size, this process is fast, in the μs range or below. Second, through shear stress, with a rate $\Gamma_2 \approx c_{66} k^2$. This process is much slower, because the shear modulus c_{66} is small. If we take $c_{66} \approx \frac{B\Phi_0}{16\pi\lambda^2\mu_0}$ we can find $c_{66} \propto \frac{1}{L^2}$ and time scales three order of magnitude above estimation, but still of the order of a small fraction of a s. A typical cooling procedure after applying the magnetic field is certainly much slower, of the order of one s.

Therefore, we conclude that we do not identify a strong effect of fluctuations and that we are instead observing the sole effect of pinning in our experiments.

-
- ¹ Brandt, E. H. & Essmann, U. The flux line lattice in type II superconductors. *Phys. Stat. Sol.(b)* **144**, 13 (1987). URL <https://doi.org/10.1002/pssb.2221440103>.
- ² Blatter, G., Feigel'man, M., Geshkenbein, V., Larkin, A. & Vinokur, V. Vortices in high temperature superconductors. *Rev. Mod. Phys.* **66**, 1125 (1994). URL <https://doi.org/10.1103/RevModPhys.66.1125>.
- ³ Pasquini, G., Daroca, D. P., Chilotte, C., Lozano, G. S. & Bekeris, V. Ordered, disordered, and coexistent stable vortex lattices in nbse₂ single crystals. *Phys. Rev. Lett.* **100**, 247003 (2008). URL <https://link.aps.org/doi/10.1103/PhysRevLett.100.247003>.
- ⁴ Guillamón, I. *et al.* Enhancement of long-range correlations in a 2D vortex lattice by an incommensurate 1D disorder potential. *Nature Physics* **10**, 1–12 (2014). URL <http://www.nature.com/doi/10.1038/nphys3132>. arXiv:1410.7782v1.
- ⁵ Fasano, Y. *et al.* Order-disorder phase transition in nbse₂ : absence of amorphous vortex matter. *Phys. Rev. B* **66**, 020512 (2002). URL <https://link.aps.org/doi/10.1103/PhysRevB.66.020512>.
- ⁶ Babaev, E. & Speight, M. Semi-meissner state and neither type-I nor type-II superconductivity in multicomponent superconductors. *Phys. Rev. B* **72**, 180502 (2005). URL <http://link.aps.org/doi/10.1103/PhysRevB.72.180502>.
- ⁷ Prozorov, R., Fidler, A. F., Hoberg, J. R. & Canfield, P. C. Suprafroth in type-I superconductors. *Nature Physics* **4**, 327–332 (2008). URL <http://dx.doi.org/10.1038/nphys888>.
- ⁸ Moshchalkov, V. *et al.* Type-1.5 superconductivity. *Phys. Rev. Lett.* **102**, 117001 (2009). URL <http://link.aps.org/doi/10.1103/PhysRevLett.102.117001>.
- ⁹ Nishio, T. *et al.* Scanning squid microscopy of vortex clusters in multiband superconductors. *Phys. Rev. B* **81**, 020506 (2010). URL <http://link.aps.org/doi/10.1103/PhysRevB.81.020506>.
- ¹⁰ Hicks, C. W. *et al.* Limits on superconductivity-related magnetization in Sr₂RuO₄ and PrOs₄Sb₁₂ from scanning squid microscopy. *Phys. Rev. B* **81**, 214501 (2010). URL <https://link.aps.org/doi/10.1103/PhysRevB.81.214501>.
- ¹¹ Silaev, M. & Babaev, E. Microscopic theory of type-1.5 superconductivity in multiband systems. *Phys. Rev. B* **84**, 094515 (2011). URL <https://link.aps.org/doi/10.1103/PhysRevB.84.094515>.
- ¹² Kogan, V. G. & Schmalian, J. Ginzburg-landau theory of two-band superconductors: Absence of type-1.5 superconductivity. *Phys. Rev. B* **83**, 054515 (2011). URL <https://link.aps.org/doi/10.1103/PhysRevB.83.054515>.
- ¹³ Babaev, E., Carlström, J. & Speight, M. Type-1.5 superconducting state from an intrinsic proximity effect in two-band superconductors. *Phys. Rev. Lett.* **105**, 067003 (2010). URL <https://link.aps.org/doi/10.1103/PhysRevLett.105.067003>.

- ¹⁴ Brandt, E. H. & Das, M. P. Attractive vortex interaction and the intermediate-mixed state of superconductors. *Journal of Superconductivity and Novel Magnetism* **24**, 57–67 (2011). URL <http://dx.doi.org/10.1007/s10948-010-1046-8>.
- ¹⁵ Gutierrez, J. *et al.* Scanning hall probe microscopy of unconventional vortex patterns in the two-gap MgB₂ superconductor. *Phys. Rev. B* **85**, 094511 (2012). URL <http://link.aps.org/doi/10.1103/PhysRevB.85.094511>.
- ¹⁶ Reimann, T. *et al.* Visualizing the morphology of vortex lattice domains in a bulk type-II superconductor. *Nature Communications* **6**, 8813 EP – (2015). URL <https://doi.org/10.1038/ncomms9813>.
- ¹⁷ Imai, Y. *et al.* Superconductivity at 5.4 k in β -Bi₂Pd. *Journal of the Physical Society of Japan* **81**, 113708 (2012). URL <http://dx.doi.org/10.1143/JPSJ.81.113708>.
- ¹⁸ Herrera, E. *et al.* Magnetic field dependence of the density of states in the multiband superconductor β -Bi₂Pd. *Phys. Rev. B* **92**, 054507 (2015). URL <http://link.aps.org/doi/10.1103/PhysRevB.92.054507>.
- ¹⁹ Kačmarčík, J. *et al.* Single-gap superconductivity in β -Bi₂Pd. *Phys. Rev. B* **93**, 144502 (2016). URL <http://link.aps.org/doi/10.1103/PhysRevB.93.144502>.
- ²⁰ Vasyukov, D. *et al.* Scanning nano-squid with single electron spin sensitivity. *Nature Nanotechnology* **8**, 639–644 (2013). URL <http://dx.doi.org/10.1038/nnano.2013.169>.
- ²¹ Halbertal, D. *et al.* Nanoscale thermal imaging of dissipation in quantum systems. *Nature* **539**, 407–410 (2016). URL <http://www.nature.com/doi/10.1038/nature19843>.
- ²² Correa, A. *et al.* Attractive interaction between superconducting vortices in tilted magnetic fields. *Communications Physics* **2**, 31 (2019). URL <https://doi.org/10.1038/s42005-019-0132-x>.
- ²³ Bolecek, N. R. C. *et al.* Vortex matter freezing in Bi₂Sr₂CaCu₂O₈ samples with a very dense distribution of columnar defects. *Phys. Rev. B* **93**, 054505 (2016). URL <https://link.aps.org/doi/10.1103/PhysRevB.93.054505>.
- ²⁴ Labusch, R. Elasticity effects in type-II superconductors. *Phys. Rev.* **170**, 470–474 (1968). URL <https://link.aps.org/doi/10.1103/PhysRev.170.470>.
- ²⁵ Johansen, T. Flux-pinning-induced stress and magnetostriction in bulk superconductors. *Supercond. Sci. Technol.* **13**, R121 (2000). URL <https://iopscience.iop.org/article/10.1088/0953-2048/13/10/201/pdf>.
- ²⁶ Lin, S.-Z. & Kogan, V. G. Strain-induced intervortex interaction and vortex lattices in tetragonal superconductors. *Phys. Rev. B* **95**, 054511 (2017). URL <https://link.aps.org/doi/10.1103/PhysRevB.95.054511>.
- ²⁷ Kogan, V. G., Bulaevskii, L. N., Miranović, P. & Dobrosavljević-Grujić, L. Vortex-induced strain and flux lattices in anisotropic superconductors. *Phys. Rev. B* **51**, 15344–15350 (1995). URL <https://link.aps.org/doi/10.1103/PhysRevB.51.15344>.
- ²⁸ Kogan, V. G. Vortex-induced strain and magnetization in type-II superconductors. *Phys. Rev. B* **87**, 020503 (2013). URL <https://link.aps.org/doi/10.1103/PhysRevB.87.020503>.
- ²⁹ Cano, A., Levanyuk, A. P. & Minyukov, S. A. Elasticity-driven interaction between vortices in type-II superconductors. *Phys. Rev. B* **68**, 144515 (2003). URL <https://link.aps.org/doi/10.1103/PhysRevB.68.144515>.
- ³⁰ Pristáš, G. *et al.* Pressure effect on the superconducting and the normal state of β -Bi₂Pd. *Phys. Rev. B* **97**, 134505 (2018). URL <https://link.aps.org/doi/10.1103/PhysRevB.97.134505>.
- ³¹ Zhao, K. *et al.* Chemical doping and high-pressure studies of layered β -PdBi₂ single crystals. *Phys. Rev. B* **92**, 174404 (2015). URL <https://link.aps.org/doi/10.1103/PhysRevB.92.174404>.
- ³² Tinkham, M. *Introduction to Superconductivity* (McGraw-Hill International Editions, 1996).
- ³³ Vacher, R., Woignier, T., Pelous, J. & Courtens, E. Structure and self-similarity of silica aerogels. *Phys. Rev. B* **37**, 6500–6503 (1988). URL <https://link.aps.org/doi/10.1103/PhysRevB.37.6500>.
- ³⁴ Pietronero, L. The fractal structure of the universe: Correlations of galaxies and clusters and the average mass density. *Physica A: Statistical Mechanics and its Applications* **144**, 257 – 284 (1987). URL <http://www.sciencedirect.com/science/article/pii/0378437187901919>.
- ³⁵ Mühlbauer, S. *et al.* Morphology of the superconducting vortex lattice in ultrapure niobium. *Phys. Rev. Lett.* **102**, 136408 (2009). URL <https://doi.org/10.1103/PhysRevLett.102.136408>.
- ³⁶ Pogosov, W. V., Misko, V. R., Zhao, H. J. & Peeters, F. M. Collective vortex phases in periodic plus random pinning potential. *Phys. Rev. B* **79**, 014504 (2009). URL <https://link.aps.org/doi/10.1103/PhysRevB.79.014504>.
- ³⁷ Ray, D., Olson Reichhardt, C. J., Jankó, B. & Reichhardt, C. Strongly enhanced pinning of magnetic vortices in type-II superconductors by conformal crystal arrays. *Phys. Rev. Lett.* **110**, 267001 (2013). URL <https://link.aps.org/doi/10.1103/PhysRevLett.110.267001>.
- ³⁸ Menezes, R. M. & Silva, C. C. d. S. Conformal vortex crystals. *Scientific Reports* **7**, 12766 (2017). URL <https://doi.org/10.1038/s41598-017-12807-4>.
- ³⁹ Romero-Isart, O., Clemente, L., Navau, C., Sanchez, A. & Cirac, J. I. Quantum magnetomechanics with levitating superconducting microspheres. *Phys. Rev. Lett.* **109**, 147205 (2012). URL <https://link.aps.org/doi/10.1103/PhysRevLett.109.147205>.
- ⁴⁰ Romero-Isart, O., Navau, C., Sanchez, A., Zoller, P. & Cirac, J. I. Superconducting vortex lattices for ultracold atoms. *Phys. Rev. Lett.* **111**, 145304 (2013). URL <https://link.aps.org/doi/10.1103/PhysRevLett.111.145304>.
- ⁴¹ Gömör, F. *et al.* Experimental realization of a magnetic cloak. *Science* **335**, 1466–1468 (2012). URL <https://science.sciencemag.org/content/sci/335/6075/1466.full.pdf>.
- ⁴² Fu, L. & Kane, C. L. Superconducting proximity effect and Majorana fermions at the surface of a topological insulator. *Phys. Rev. Lett.* **100**, 096407 (2008). URL <https://link.aps.org/doi/10.1103/PhysRevLett.100.096407>.
- ⁴³ Xu, J.-P. *et al.* Experimental detection of a majorana mode in the core of a magnetic vortex inside a topological insulator-superconductor Bi₂Te₃/NbSe₂ Heterostructure. *Phys. Rev. Lett.* **114**, 017001 (2015). URL <https://link.aps.org/doi/10.1103/PhysRevLett.114.017001>.

- ⁴⁴ Wang, D. *et al.* Evidence for majorana bound states in an iron-based superconductor. *Science* **362**, 333–335 (2018). URL <https://science.sciencemag.org/content/362/6412/333>.
- ⁴⁵ Demirdiř, S. *et al.* Strong pinning and vortex energy distributions in single-crystalline $\text{Ba}(\text{Fe}_{1-x}\text{Co}_x)_2\text{As}_2$. *Phys. Rev. B* **84**, 094517 (2011). URL <https://link.aps.org/doi/10.1103/PhysRevB.84.094517>.
- ⁴⁶ Demirdiř, S. *et al.* Disorder, critical currents, and vortex pinning energies in isovalently substituted $\text{BaFe}_2(\text{As}_{1-x}\text{P}_x)_2$. *Phys. Rev. B* **87**, 094506 (2013). URL <https://link.aps.org/doi/10.1103/PhysRevB.87.094506>.
- ⁴⁷ Galvis, J. A. *et al.* Three axis vector magnet set-up for cryogenic scanning probe microscopy. *Review of Scientific Instruments* **86**, 013706 (2015). URL <http://scitation.aip.org/content/aip/journal/rsi/86/1/10.1063/1.4905531>.
- ⁴⁸ Lachman, E. O. *et al.* Visualization of superparamagnetic dynamics in magnetic topological insulators. *Science Advances* **1**, e1500740 (2015). URL <https://advances.sciencemag.org/content/advances/1/10/e1500740.full.pdf>.
- ⁴⁹ Anahory, Y. *et al.* Emergent nanoscale superparamagnetism at oxide interfaces. *Nature Communications* **7**, 12566 (2016). URL <http://www.nature.com/doi/10.1038/ncomms12566>.
- ⁵⁰ Embon, L. *et al.* Probing dynamics and pinning of single vortices in superconductors at nanometer scales. *Scientific Reports* **5**, 7598 (2015). URL <https://www.nature.com/articles/srep07598.pdf>.
- ⁵¹ Embon, L. *et al.* *Nature Communications* **8**, 85 (2017). URL <https://www.nature.com/articles/s41467-017-00089-3>.
- ⁵² Huber, M. E. *et al.* DC squid series array amplifiers with 120 MHz bandwidth (corrected). *IEEE Transactions on Applied Superconductivity* **11**, 4048–4053 (2001). URL <https://ieeexplore.ieee.org/stamp/stamp.jsp?tp=&arnumber=947383>.
- ⁵³ Ginzburg, V. L. Some remarks concerning the macroscopic theory of superconductivity. *Sov. Phys. JETP* **3**, 621 (1956). URL http://www.jetp.ac.ru/cgi-bin/dn/e_003_04_0621.pdf.
- ⁵⁴ Doria, M. M., Gubernatis, J. E. & Rainer, D. Virial theorem for ginzburg-landau theories with potential applications to numerical studies of type-II superconductors. *Phys. Rev. B* **39**, 9573 (1989). URL <https://journals.aps.org/prb/pdf/10.1103/PhysRevB.39.9573>.
- ⁵⁵ The code is available at github. URL <https://github.com/LowTemperaturesUAM/MultiFractal-Analysis>.
- ⁵⁶ Shein, I. & Ivanovskii, A. Electronic band structure and fermi surface of tetragonal low-temperature superconductor bi_2pd as predicted from first principles. *Journal of Superconductivity and Novel Magnetism* **26**, 1–4 (2013). URL <http://dx.doi.org/10.1007/s10948-012-1776-x>.
- ⁵⁷ Novoselov, K. S. *et al.* Two-dimensional atomic crystals. *Proceedings of the National Academy of Sciences* **102**, 10451–10453 (2005).
- ⁵⁸ Sakano, M. *et al.* Topologically protected surface states in a centrosymmetric superconductor $\beta - \text{pdbi}_2$. *Nature Communications* **6**, 8595 (2015). URL <http://www.nature.com/articles/ncomms9595#supplementary-information>.
- ⁵⁹ Iwaya, K. *et al.* Full-gap superconductivity in spin-polarised surface states of topological semimetal $\beta\text{-PdBi}_2$. *Nature Communications* **8**, 976 (2017). URL <https://doi.org/10.1038/s41467-017-01209-9>.
- ⁶⁰ Zehnder, A. T. Fracture mechanics. *Lecture notes in applied and computational mechanics* **62** (2012).
- ⁶¹ Mecholsky, J. J. Fractography: Determining the sites of fracture initiation. *Dental Materials* **11**, 113 – 116 (1995). URL <http://www.sciencedirect.com/science/article/pii/010956419580045X>.
- ⁶² Hauch, J. A., Holland, D., Marder, M. P. & Swinney, H. L. Dynamic fracture in single crystal silicon. *Phys. Rev. Lett.* **82**, 3823–3826 (1999). URL <https://link.aps.org/doi/10.1103/PhysRevLett.82.3823>.
- ⁶³ Guo, Y. *et al.* Distinctive in-plane cleavage behaviors of two-dimensional layered materials. *ACS Nano* **10**, 8980–8988 (2016).
- ⁶⁴ Kermod, J. R. *et al.* Macroscopic scattering of cracks initiated at single impurity atoms. *Nature Communications* **4**, 2441 EP – (2013). URL <http://dx.doi.org/10.1038/ncomms3441>.
- ⁶⁵ Marx, M., Schaefer, W. & Vehoff, H. Interaction of short cracks with the local microstructure. *Procedia Engineering* **2**, 163 – 171 (2010). URL <http://www.sciencedirect.com/science/article/pii/S1877705810000196>.
- ⁶⁶ Shein, I. R. & Ivanovskii, A. L. Electronic band structure and fermi surface of tetragonal low-temperature superconductor bi_2pd as predicted from first principles. *Journal of Superconductivity and Novel Magnetism* **26**, 1–4 (2013). URL <http://dx.doi.org/10.1007/s10948-012-1776-x>.
- ⁶⁷ Coldea, A. *private communication*.
- ⁶⁸ Lv, Y.-F. *et al.* Experimental Observation of Topological Superconductivity and Majorana Zero Modes on beta-Bi₂Pd Thin Films. *Science Bulletin* **62**, 852 (2017). URL <https://doi.org/10.1016/j.scib.2017.05.008>.
- ⁶⁹ Caroli, C., Gennes, P. D. & Matricon, J. Bound fermion states on a vortex line in a type II superconductor. *Physics Letters* **9**, 307 – 309 (1964).
- ⁷⁰ Hess, H. F., Robinson, R. B. & Waszczak, J. V. Vortex-core structure observed with a scanning tunneling microscope. *Phys. Rev. Lett.* **64**, 2711–2714 (1990). URL <http://link.aps.org/doi/10.1103/PhysRevLett.64.2711>.
- ⁷¹ Guillamon, I., Suderow, H., Guinea, F. & Vieira, S. Intrinsic atomic-scale modulations of the superconducting gap of 2h-nbse_2 . *Phys. Rev. B* **77**, 134505 (2008). URL <http://link.aps.org/doi/10.1103/PhysRevB.77.134505>.
- ⁷² Li, Y., Xu, X. & Chien, C. L. Observation of Half-Quantum Flux in Unconventional Superconductor $\beta\text{-Bi}_2\text{Pd}$. *ArXiv e-prints* (2018). 1810.11265.
- ⁷³ Vollhardt, D. & Woelfle, P. *The Superfluid Phases Of Helium 3* (Taylor and Francis, 1990).
- ⁷⁴ Goldobin, E., Koelle, D. & Kleiner, R. Ground states of one and two fractional vortices in long josephson $0-\kappa$ junctions. *Phys. Rev. B* **70**, 174519 (2004). URL <https://link.aps.org/doi/10.1103/PhysRevB.70.174519>.
- ⁷⁵ Kirtley, J. R. *et al.* Direct imaging of integer and half-integer josephson vortices in high- T_c grain boundaries. *Phys. Rev. Lett.* **76**, 1336–1339 (1996). URL <https://link.aps.org/doi/10.1103/PhysRevLett.76.1336>.
- ⁷⁶ Gurevich, A. *Phys. Rev. B* **48**, 12857 (1993). URL <https://doi.org/10.1103/PhysRevB.48.12857>.
- ⁷⁷ Brun, C. *et al.* *Nature Physics* **10**, 444 (2014). URL <https://www.nature.com/articles/nphys2937.pdf>.

- ⁷⁸ Zheng, J. & Margine, E. Electron-phonon coupling and pairing mechanism in bi2pd centrosymmetric superconductor. *Phys. Rev. B* **95**, 014512 (2017). URL <https://link.aps.org/doi/10.1103/PhysRevB.95.014512>.
- ⁷⁹ Träuble, H. & Essmann, U. Fluxline arrangement in superconductors as revealed by direct observation. *Journal of Applied Physics* **39**, 4052–4059 (1968).
- ⁸⁰ Hubener, R. *Magnetic Flux Structures in Superconductors* (Springer,, 2001).
- ⁸¹ Fasano, Y. & Menghini, M. Magnetic-decoration imaging of structural transitions induced in vortex matter. *Superconductor Science and Technology* **21**, 023001 (2008). URL <http://stacks.iop.org/0953-2048/21/i=2/a=023001>.
- ⁸² Aston, D. R., Dubeck, L. W. & Rothwarf, F. "intermediate mixed" state of type-II superconductors. *Phys. Rev. B* **3**, 2231–2236 (1971). URL <http://link.aps.org/doi/10.1103/PhysRevB.3.2231>.
- ⁸³ Ge, J.-Y. *et al.* *Phys. Rev. B* **90**, 184511 (2014). URL <https://journals.aps.org/prb/abstract/10.1103/PhysRevB.90.184511>.
- ⁸⁴ Schmucker, R. & Brandt, E. H. *physica status solidi (b)* **79**, 479–487 (1977).
- ⁸⁵ Varlamov, A. A., Galda, A. & Glatz, A. Fluctuation spectroscopy: From rayleigh-jeans waves to abrikosov vortex clusters. *Rev. Mod. Phys.* **90**, 015009 (2018). URL <https://link.aps.org/doi/10.1103/RevModPhys.90.015009>.
- ⁸⁶ Houghton, A., Pelcovits, R. A. & Sudbø, A. Elastic modes, phase fluctuations, and long-range order in type-II superconductors. *Phys. Rev. B* **42**, 906–908 (1990). URL <https://link.aps.org/doi/10.1103/PhysRevB.42.906>.
- ⁸⁷ Feigel'man, M. V. & Vinokur, V. M. Thermal fluctuations of vortex lines, pinning, and creep in high- t_c superconductors. *Phys. Rev. B* **41**, 8986–8990 (1990). URL <https://link.aps.org/doi/10.1103/PhysRevB.41.8986>.
- ⁸⁸ Moore, M. A. Destruction by fluctuations of superconducting long-range order in the abrikosov flux lattice. *Phys. Rev. B* **39**, 136–139 (1989). URL <https://link.aps.org/doi/10.1103/PhysRevB.39.136>.
- ⁸⁹ Brandt, E. H. Thermal fluctuation and melting of the vortex lattice in oxide superconductors. *Phys. Rev. Lett.* **63**, 1106–1109 (1989). URL <https://link.aps.org/doi/10.1103/PhysRevLett.63.1106>.
- ⁹⁰ Marchetti, M. C. & Nelson, D. R. Dislocation loops and bond-orientational order in the abrikosov flux-line lattice. *Phys. Rev. B* **41**, 1910–1920 (1990). URL <https://link.aps.org/doi/10.1103/PhysRevB.41.1910>.
- ⁹¹ Marchetti, M. C. & Nelson, D. R. Hydrodynamics of flux liquids. *Phys. Rev. B* **42**, 9938–9943 (1990). URL <https://link.aps.org/doi/10.1103/PhysRevB.42.9938>.
- ⁹² Koshelev, A. E. & Kes, P. H. Collective-pinning theory for magnetically coupled layered superconductors. *Phys. Rev. B* **48**, 6539–6549 (1993). URL <https://link.aps.org/doi/10.1103/PhysRevB.48.6539>.
- ⁹³ Brandt, E. H. Elastic and plastic properties of the flux-line lattice in type-II superconductors. *Phys. Rev. B* **34**, 6514–6517 (1986). URL <https://link.aps.org/doi/10.1103/PhysRevB.34.6514>.
- ⁹⁴ Bulaevskii, L. N. & Maley, M. P. Low temperature specific heat of the vortex lattice in layered superconductors. *Phys. Rev. Lett.* **71**, 3541–3544 (1993). URL <https://link.aps.org/doi/10.1103/PhysRevLett.71.3541>.